A Descriptive Force-Balance Model for Droplet Formation at Microfluidic Y-Junctions

Maartje L. J. Steegmans, Jolet De Ruiter, Karin G. P. H. Schroën, and Remko M. Boom
Food Engineering Group, Dept. ATV, Wageningen University, 6700 EV Wageningen, The Netherlands

DOI 10.1002/aic.12176
Published online January 20, 2010 in Wiley Online Library (wileyonlinelibrary.com).

In a previous article, we studied the basics of emulsification in microfluidic Y-junctions, however, without considering the effect of viscosity of the disperse phase. As it is known from investigations on many different microstructures that viscosity and viscosity ratio are governing parameters for droplet size, we here investigate whether this is also the case for microfluidic Y-junctions and do so for a wide range of process conditions. The investigated Y-junctions have a width of 19.9 or 12.8 μm and a depth of 5.0 μm, and the formed monodisperse droplets (CV < 1%) are between 3 and 20 μm. We varied the disperse-phase viscosity using different oils (1–105 mPa s), and continuous-phase viscosity using glycerol–water and ethanol–water mixtures (1.0–6.2 mPa s), which corresponds to disperse-to-continuous-phase viscosity ratios from 0.4 to 105.0. Through the variation of the liquids, also a range in interfacial tensions (12–55 mN m^{-1}) is assessed. The disperse-phase flow rate is varied from 0.039 to 18.0 μL h^{-1}, the continuous-phase flow rate from 1.39 μL h^{-1} to 0.41 mL h^{-1}, and this corresponds to flow rate ratios from 1.1 × 10^{-3} to 0.14, which is once again based on wide range of conditions. For all these conditions, in which droplets are formed in the dripping and jetting regime, the droplet size could be described with a model based on the existing force-balance model, but now extended to incorporate the cross-sectional area of the droplet and the resistance with the wall. Surprisingly enough, it was found that the droplet size is not influenced by the disperse-phase viscosity, or the viscosity ratio, but it is dominated by the resistance with the wall and the continuous-phase properties. Because of this, emulsification with Y-junctions is intrinsically simpler than any other shear-based method as droplet size is only determined by the continuous phase. © 2010 American Institute of Chemical Engineers *AIChE J,* 56: 2641–2649, 2010

Keywords: emulsion, droplet size, microchannel, wall effects, viscosity, force-balance model

Introduction

Traditionally, emulsions are prepared with mixers, rotor-stator systems, ultrasonic, or high-pressure homogenizers.[1–3] With these techniques, droplets are formed by elongation and shear, which generally results in a broad droplet size distribution. Therefore, microfluidic emulsification has gained attention, as the produced emulsion droplets are monodisperse.

Microfluidic emulsification includes various geometries with typical channel sizes in the order of several to hundreds of micrometers. The observed droplet-formation mechanism depends on the geometry. One of the most extensively studied shear-driven microfluidic geometries is the T-junction.[4–10] At T-junctions, droplet formation can be described with a two-step droplet formation model consisting of a droplet

Correspondence concerning this article should be addressed to M. L. J. Steegmans at maartje.steegmans@wur.nl.

growth and a droplet detachment step, as we found to be the case in a review of all available articles on T-junctions.[11] As in T-junctions, droplet formation is rather complex, in this article we prefer emulsification at microfluidic Y-junctions,[12–15] in which droplet formation takes place through a much simpler one-step mechanism.[15] Because of this, variation of a process parameter is expected to have a direct and more easily traceable effect on the droplet size.

In our previous article, we discovered that emulsification at (flat) Y-junctions is much simpler than in other (shear-driven) microfluidic geometries, as the droplet size is independent of the disperse-phase flow rate as it operates through a one-step mechanism.[15] In the dripping and jetting regime, droplet size could be described with a force balance between the interfacial tension force and the shear force at the position where the neck and the incipient droplet are connected.[15] The interfacial tension force is the main force keeping the incipient droplet attached to the bulk, and it acts opposite to the shear force exerted by the continuous phase. The derived force-balance model was validated for a fairly wide range of interfacial tensions and flow rates, even though for only one disperse-phase viscosity and a rather limited range of continuous-phase viscosities.[15] As it is noted in literature[9,16–18] that viscosity of both phases, viscosity ratio, flow rates, and flow rate ratios can be of imminent importance for emulsification (in microfluidic devices), this was investigated further for Y-junctions. We varied the disperse-phase and continuous-phase viscosity, corresponding to viscosity ratios from 0.4 to 105.0, and disperse-phase and continuous-phase flow rates, corresponding to flow rate ratios from 1.1×10^{-3} to 0.14. For this wide range of process conditions, the droplet sizes were compared with our existing force-balance model and various extended models, (i.e., that include wall effects), and on the basis of this analysis, the ruling parameters for droplet formation in Y-junctions were identified.

Experimental

Materials

Disperse Phases. *n*-Hexadecane (anhydrous, purity >99%, no. 296317, Sigma-Aldrich, Steinheim, Germany), low-viscous paraffin oil (no. 1.07174.1000, Merck, Darmstadt, Germany), high-viscous paraffin oil (no. 1.07160.1000, Merck, Darmstadt, Germany), 40 wt % pentane–hexadecane, or 60 wt % capric acid–hexadecane mixtures were used as disperse phase. The mixtures were prepared from *n*-hexadecane and *n*-pentane (no. 1.07177.1000, Merck, Darmstadt, Germany) or capric acid (purity ≥98%, no. C1875, Sigma, Zwijndrecht, The Netherlands), respectively. Before use, the paraffin oils and 60 wt % capric acid–hexadecane mixture were filtered with a hydrophobic 0.2 μm filter (no. 10463503, Whatman, Dassel, Germany). To prevent crystallization, the 60 wt % capric acid–hexadecane mixture was heated up to 40°C and cooled down to 23°C just before use.

Continuous Phases. Milli-Q water, 20, 30, 50 wt % glycerol–water, 9, or 28 wt % ethanol–water mixtures were used as the continuous phase. The glycerol–water mixtures were prepared from Milli-Q water and glycerol (purity ≥99.5%, no. 49767, Fluka, Buchs, Switzerland) and were filtered with a hydrophilic 0.2 μm filter (no. 62131, Alltech, Deerfield). The ethanol–water mixtures were prepared from Milli-Q water and 96% v/v ethanol (no. 20824, VWR BDH Prolabo, Amsterdam, The Netherlands).

Viscosity. The viscosities of the Newtonian continuous and disperse phases were measured in duplicate in a rheometer (MCR 301, Anton Paar, Graz, Austria) with a Couette geometry (DG 26.7, Anton Paar, Graz, Austria) (see Table 1). For each measurement, forward and backward rate sweep were performed between 1 and 900 s^{-1} at a controlled temperature of 23°C. Each of the 18 shear rates was applied for at least 6 s (900 s^{-1}) up to 30 s (1 s^{-1}) and measurement occurred at the end of each period.

Density. The densities of the phases were determined in duplicate with a calibrated 49.960 mL Gay-Lussac-type pyknometer (Brand, Wertheim, Germany) at a controlled temperature of 23°C (see Table 1).

Static Interfacial Tension. The static interfacial tensions (see Table 2) between the various continuous and disperse phases were measured in duplicate at a controlled temperature of 23°C using a dynamic drop tensiometer (ADT, ITCONCEPT, Longessaigne, France).[19] A disperse-phase droplet between 5 and 10 μL was formed at the tip of a U-shaped needle positioned in a cuvette with the continuous phase; to prevent premature droplet detachment the droplet volume was decreased with decreasing interfacial tension. The interfacial tension was determined by droplet shape analysis as described by Benjamins et al.[19] The samples were measured in the order of increasing concentration of the continuous phase, and after each concentration, the cuvette and the needle were rinsed extensively with Milli-Q water. Between the various disperse phases and glycerol– and ethanol–water mixtures, the cuvette and the needle were rinsed with hot tap water, chloroform, tap water, and Milli-Q water.

Experimental setup

Microfluidic Y-Junction Device. We designed borosilicate glass microfluidic devices with Y-junctions, subsequently produced by Micronit Microfluidics BV (Enschede, The Netherlands) (for further details see Steegmans et al.[15]).

Table 1. Viscosity η and Density ρ of the Various Phases at a Temperature of 23°C

Sample*	η (mPa s)	ρ (kg m^{-3})
Disperse phases		
Pentane–hexadecane 40 wt % (PHD40)	1.0	710
Hexadecane (HD)	3.5	773
Capric acid–hexadecane 60 wt % (CAHD60)	6.4	839
Low-viscous paraffin oil (LPO)	29.8	848
High-viscous paraffin oil (HPO)	105.0	860
Continuous phases		
Milli-Q water (M)	1.0	996
Glycerol–water 20 wt % (G20)	1.8	1045
Glycerol–water 30 wt % (G30)	2.6	1071
Glycerol–water 50 wt % (G40)	6.2	1124
Ethanol–water 9 wt % (E9)	1.5	980
Ethanol–water 28 wt % (E28)	2.5	954

*The abbreviations used for the various liquids in this article are given between brackets.

Table 2. Static Interfacial Tension γ (in mN m^{-1}) at a Temperature of 23°C

Continuous Phase	M	G20*	G30	G50*	E9*	E28*
Disperse phase						
PHD40	41	–	37	–	–	–
HD	41	37	35	34	27	15
CAHD60	12	–	12	12	–	–
LPO	49	–	45	39	–	–
HPO	55	–	44	–	–	–

*A dash means that the static interfacial tension was not measured.

Figure 1. Picture of the Y-junction.

Low-viscous paraffin oil droplets are formed in 30 wt % glycerol-water at $\phi_{G30} = 89$ ($\pm$ 2) μL h^{-1} and $\phi_{LPO} = 2.5$ ($\pm$ 0.1) μL h^{-1}.

All intervals given in this article for the continuous- and disperse-phase flow rate are derived from image analysis assuming a maximal experimental error of one pixel or one frame.

The microfluidic device consists of a lower plate in which the Y-channels are (chemically) etched and which is annealed to a top plate with inlets. After enclosure, the microchannels and collecting area have a uniform depth of 5 μm.

Figure 1 shows a picture of the Y-junction. The continuous phase enters the Y-junction via channel C, whereas the disperse phase enters via channel D. The angle between channels C and D is 97°. At the Y-junction, both phases meet and droplets are formed, which are transported through channel E toward the collecting area. Except for one device, channel width was between 18 and 20 μm (see Table 3).

Droplet-Formation Experiments. The Y-junction devices were operated in the appropriate holder (no. 4515, Micronit Microfluidics BV, Enschede, The Netherlands), and the continuous and disperse phase were supplied as described in previous work.[15] At applied continuous-phase flow rates ranging from 0.01 to 0.80 mL h^{-1} and applied disperse-phase flow rates ranging from 0.2 μL h^{-1} to 0.20 mL h^{-1}, droplets were formed at the Y-junction. The actual flow rates at the Y-junction were found to differ from the (applied) flow rates set on the pump, probably because of the large pressure drop in the microfluidic device (in the order of tens of bars). Therefore, the continuous- and disperse-phase flow rates were calculated (for details on the calculation see Steegmans et al.[15]). The actual continuous-phase flow rate used for further analysis was calculated in the range from 1.39 μL h^{-1} to 0.41 mL h^{-1}, and from 0.039 to 18.0 μL h^{-1} for the disperse phase. This corresponds to a disperse-to-continuous-phase-flow-rate-ratios from 1.1×10^{-3} to 0.14. After changing the flow rate(s), the droplet-formation process was allowed to equilibrate for at least 2 min.

Droplet formation in the dripping and jetting regime was recorded using a high-speed camera (MotionPro HS-4, Redlake, Tallahassee) connected to an inverted transmitted light microscope (Axiovert 200, Carl Zeiss, Sliedrecht, The Netherlands). The formation of 25 subsequent hexadecane droplets was recorded using ~20 frames per droplet, which corresponds to frame rates between 210 and 73,502 s^{-1}. The gain and the exposure time were chosen such that the image quality was optimal.

Analysis

Droplet Size. The hexadecane droplet size was determined automatically using a custom-written script based on the DIPimage toolbox operating in Matlab 7.0.1. The area of each droplet was determined as the average over three subsequent frames. Ten subsequent droplets were measured; the reported size was the average of these 10 with a 95% confidence interval (average $\pm$ 1.96·standard deviation).

The droplet volume V was calculated from the droplet area. When the diameter of the droplet was smaller than the depth of the microchannel, the droplet was spherical (drop); otherwise, the droplet was squeezed in between the bottom and top surface and disc-shaped (disc) as shown in Figure 2 of our previous article.[15] The volume V of discs was calculated assuming rounded edges with the channel depth as curvature[15]:

Table 3. Width of the Continuous-Phase Channel w_c, Disperse-Phase Channel w_D, and Downstream Channel w_E as Measured with Image Analysis of the Studied Microfluidic Y-Junctions

Disperse Phase	Continuous Phase	w_c (μm)	w_D (μm)	w_E (μm)
PHD40	M, G30	18.8	19.2	19.0
PHD40	M, G30	18.6	18.9	18.9
HD	M, E9, E28	18.0	18.2	18.1
HD	M, G20	18.2	18.1	18.1
HD	M, G20	19.4	19.8	19.7
HD	G20, G30	19.4	19.9	19.6
CAHD60	M, G30	18.7	19.1	18.9
CAHD60	G30, G50	19.0	19.1	19.1
LPO	M, G30	19.0	19.0	19.1
HPO	M, G30	19.6	19.6	19.6
HD	M, G20, G30	12.9	13.1	12.8

Widths have a measurement error of $\pm$ 0.5 μm. The depth of the Y-junctions is 5.0 μm for all devices (because of the chemical etching process used during production). The disperse and continuous phase(s) used in each Y-junction are indicated in the code.

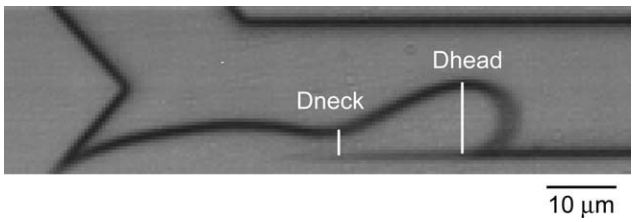

Figure 2. Picture of the second-to-last frame before low-viscous paraffin oil droplet detachment in 30 wt % glycerol with herein indicated droplet-formation quantities D_{head} and D_{neck}.

Flow rates are as stated for Figure 1.

$$V = \frac{\pi z}{4}(D-z)^2 + \frac{\pi^2 z^2}{8}\left(D - \left(1 - \frac{4}{3\pi}\right)z\right), \quad (\mathrm{m}^3) \qquad (1)$$

with D the diameter of the disc area, and z the depth of the microchannels. To compare drops and discs, the equivalent diameter D_{3D} of an unrestricted spherical droplet with the same volume as the disc was calculated ($D_{3D} = (6V/\pi)^{1/3}$) and used for further analysis.

Droplet-Formation Quantities. Two characteristic droplet-formation quantities were determined in the second-to-last frame before droplet detachment: D_{head} and D_{neck} (see Figure 2). D_{head} is the largest diameter of the incipient droplet head and D_{neck} is the width of the thinnest point of the filament keeping the droplet attached to the disperse-phase bulk (neck). The quantities were manually determined with Image-Pro Plus 4.5.0.29. For each quantity, the average of 10 incipient droplets was taken, and a corresponding 95% confidence interval was calculated.

Statistical analysis

The relation between D_{head} and D_{3D}, as described in Eq. 18, was established using the least squares method. The standard deviations of the parameters (a, b, and c) were estimated as the product of the square root of the residual mean square and the square root of the variance of the parameter. Minimal sum of squares, parameters, and standard deviations were found with the Levenberg–Marquardt method in Mathcad 14.

Results and Discussion

Critical capillary number for Y-junctions

At microfluidic Y-junctions in the dripping and jetting regime, monodisperse micron-sized droplets with a polydispersity index (standard deviation to average droplet size ratio) below 1% were formed with frequencies of 10 up to more than 10,000 droplets per second. In emulsification literature, it is common to use a critical capillary number for droplet break-up. For microfluidic Y-junctions, the determined capillary numbers [defined according to Grace[16] as: $(Ca = (\dot{\gamma}_c R_{3D}\eta_c)/\gamma$, where γ_c is the shear rate of the continuous phase, R_{3D} is the droplet radius, η_c is the viscosity of the continuous phase, and γ is the interfacial tension] for micron-sized droplets are in the order of 10^{-3} to 10^{-2} (see Figure 3). This is at least 10, but in most cases, 100 times or more lower than reported by Grace[16] for millimeter-sized emulsion droplets generated by elongation or rotation. This implies that in microfluidic Y-junctions shear is used more efficiently to form droplets than in (rotational) shear or elongation. Most probably, geometric confinement in combination with the rectangular cross-section of the channels promotes instability of the liquid column and therewith droplet break-up. Guillot et al.[20] showed that the absence of confinement in one direction, as observed for a liquid column enclosed in a channel with a rectangular cross-section (see Figure 2), promotes instability of a liquid column. Besides, Figure 3 suggests that the dependency of the critical capillary number on viscosity ratio seems less pronounced for microfluidic Y-junctions than for (rotational) shear or elongation, which might indicate viscosity ratio independency for the experimental conditions investigated here (viscosity ratio 0.4–105.0 and flow rate ratio 1.1×10^{-3}–0.14).

Droplet formation at Y-junctions

In the next sections, the effect of e.g. viscosity ratio on emulsion droplet size at microfluidic Y-junctions is studied more extensively. We start by visual observation of the droplet-formation process. Regardless of the properties of the disperse and/or the continuous phase, we observed that droplet formation starts with interface expansion without movement along the downstream channel [see Figures 4a(B)–4d(B)]. Subsequently, the tip of the disperse phase starts to move along the downstream channel in the direction of the continuous-phase flow [see Figures 4a(C)–4d(C)], until the incipient droplet is connected to the bulk with a neck [see Figures

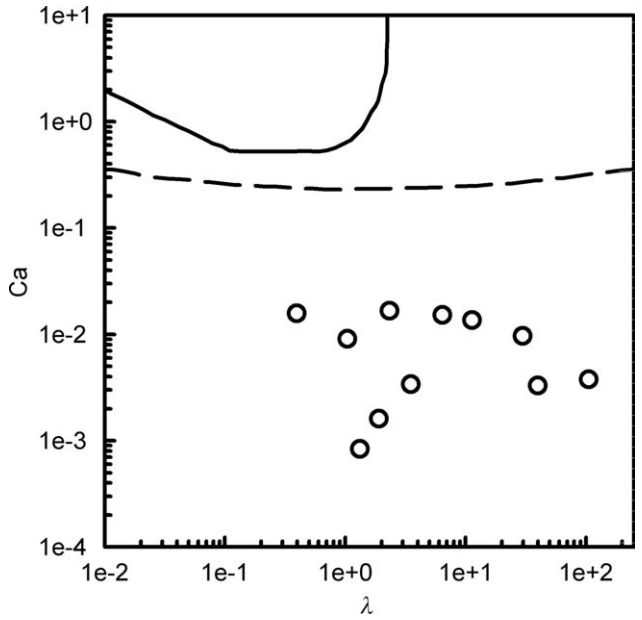

Figure 3. The critical capillary number ($Ca = (\dot{\gamma}R_{3D}\eta_c)/\gamma$) as function of the disperse-to-continuous-phase-viscosity-ratio λ.

The spheres (○) are the capillary numbers obtained in our Y-junctions for the dripping and jetting regime. The solid line is the curve for (rotational) shear flow and the dashed line is the curve for elongational flow after Grace, Figure 19.[16]

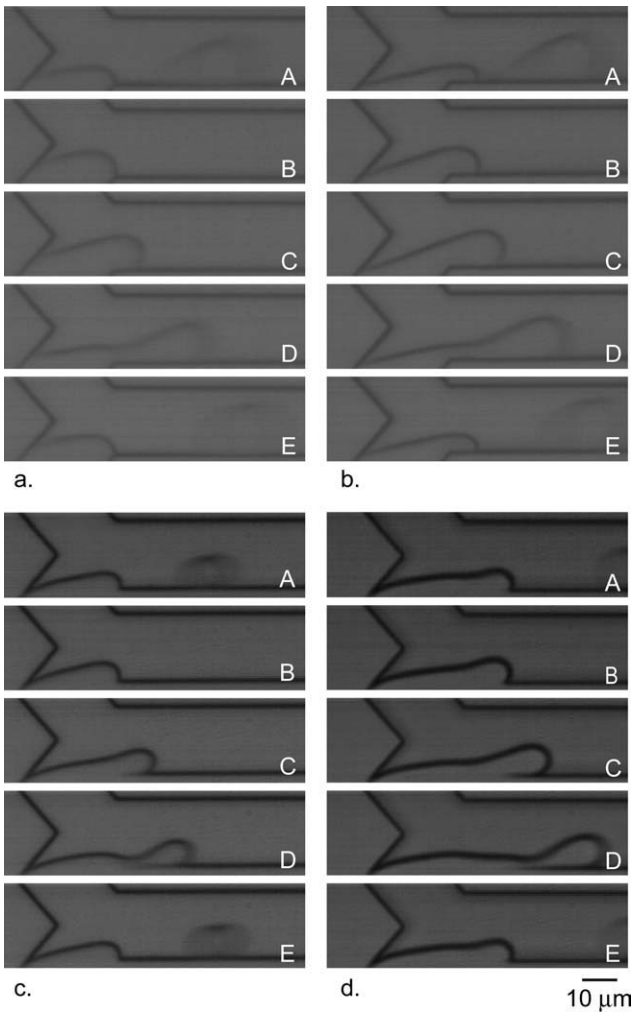

Figure 4. Droplet formation at the Y-junction (dripping, a and c) and droplet formation downstream (jetting, b and d).

For further details on the process conditions, see Table 4.

4a(D)–4d(D)]. Then, the diameter of the neck swiftly decreases and the droplet detaches, after which the interface returns to its original position [see Figures 4a(E)–4d(E)].

Emulsion droplet formation occurs either at the Y-junction (dripping, see Figures 4a, c) or downstream, near the bottom wall (jetting, see Figures 4b, d). For 40 wt % pentane–hexadecane, hexadecane, low-viscous, and high-viscous paraffin oil, monodisperse emulsion droplets were formed with both mechanisms, but for the 60 wt % capric acid–hexadecane, this occurs only downstream. We previously found that both droplet formation at the junction and downstream can be treated as one for the force-balance analysis,[15] and, therefore, in the remainder of this article the two mechanisms will not be distinguished.

Force-balance model development

To estimate the droplet size at Y-junctions for different disperse phases, we adapted the existing force-balance model[15] by redefining the interfacial tension force F_γ and the shear force F_{shear}. Abating (the swift decrease of the neck resulting in detachment) is infinitely fast in the dripping and jetting regime,[15] which implies that the eventual droplet size equals the droplet size when abating starts, i.e., when both forces are equal:

$$F_\gamma = F_{\text{shear}}. \tag{2}$$

In the next sections, the various steps that were taken to redefine the interfacial tension force and the shear force are systematically presented.

Interfacial Tension Force. The diameter of the neck was experimentally determined, and as the disperse phase tends to minimize its contact area with the continuous phase, the neck was assumed to be cylindrical (see Figure 5). The interfacial tension force can, therefore, be estimated with:

$$F_\gamma = \pi D_{\text{neck}} \gamma. \quad \text{(N)} \tag{3}$$

In a previous work,[15] we assumed that the neck diameter is approximately equal to the channel depth (5 μm), but from the current investigation, it is clear that this is not the case as shown in Figure 5c. Besides, this figure suggests that the neck diameter depends on the disperse phase, but no straightforward relation to describe this effect is available. Therefore, the experimentally determined value of D_{neck} is used when D_{neck} is below channel depth, otherwise $D_{\text{neck}} = z$, as the neck cannot start abating as long as $D_{\text{neck}} > z$.

Shear Force. The shear force is based on the general drag equation.[21] For the cross-sectional area of the incipient droplet head exposed to the continuous-phase flow (i.e., minus the area shaded by the neck, see Figure 5) in a rectangular channel, it is written:

$$F_{\text{shear}} = 1.125 \rho_c v_c^2 A_\perp K_{\text{wall}} C_D \Lambda. \quad \text{(N)} \tag{4}$$

where ρ_c is the continuous-phase density, v_c is the (average) velocity of the continuous phase along the neck calculated with Eq. 5, $A_\perp$ is the cross-sectional area of the incipient droplet head exposed to the continuous-phase flow calculated with Eq. 6 or 7, K_{wall} is the wall correction factor, C_D is the drag coefficient, and Λ is the Hadamard viscosity correction factor.[22–24] The velocity along the neck is calculated as:

$$v_c = \frac{\phi_c}{A_{\perp,E} - A_{\perp,\text{neck}}} = \frac{\phi_c}{z w_E - \frac{\pi}{4} D_{\text{neck}}^2}. \quad \text{(m s}^{-1}\text{)} \tag{5}$$

where ϕ_c is the continuous-phase flow rate, $A_{\perp,E}$ is the cross-sectional area of the downstream channel, and w_E is the downstream-channel width. The cross-sectional area of the incipient droplet head exposed to the continuous phase $A_\perp$ is calculated for $D_{\text{head}} > z$ as:

$$A_\perp = A_{\perp,\text{head}} - A_{\perp,\text{neck}} = \frac{\pi}{4}(z^2 - D_{\text{neck}}^2) + z(D_{\text{head}} - z). \quad \text{(m}^2\text{)} \tag{6}$$

and otherwise (i.e. $D_{\text{head}} \leq z$):

$$A_\perp = A_{\perp,\text{head}} - A_{\perp,\text{neck}} = \frac{\pi}{4}(D_{\text{head}}^2 - D_{\text{neck}}^2). \quad \text{(m}^2\text{)}, \tag{7}$$

Table 4. Details of the Pictures Shown in Figure 4

Picture	Disperse Phase	Continuous Phase	ϕ_d (μL h^{-1})	ϕ_c (μL h^{-1})	Time (ms) A	B	C	D	E
a	PHD40	M	9.4 ± 0.08	260 ± 8	0	0.08	0.22	0.32	0.36
b	PHD40	M	8.2 ± 0.3	210 ± 9	0	0.14	0.27	0.39	0.43
c	LPO	G30	2.2 ± 0.02	185 ± 6	0	0.11	0.43	0.54	0.60
d	LPO	M	3.3 ± 0.1	256 ± 8	0	0.07	0.4	0.6	0.67

where $A_{\perp,\text{head}}$ is the cross-sectional area of the head and $A_{\perp,\text{neck}}$ that of the neck.

Wall Correction Factor. During droplet formation, the incipient droplet head is in contact with the channel wall. When the cross-sectional area of the downstream channel is largely occupied by the head, the resistance coefficient between the head and the wall can be described with[22,25]:

$$K_{\text{wall}}(k,e) = 0.83\alpha_0(e)\left(k^{\frac{5}{2}} + (2.62+\alpha_1(e))k^{\frac{3}{2}} + (2.01+\alpha_t(e))k^{\frac{1}{2}}\right) + \ldots \quad (\text{for } k < 1) \quad (8)$$

where k is the clearance between the channel and the droplet head defined for Y-junctions as:

$$k = \frac{w_E - D_{\text{head}}}{D_{\text{head}}} \quad (9)$$

e is a measure for the position of the center of the droplet head compared to the wall, and $\alpha_0(e)$, $\alpha_1(e)$, and $\alpha_t(e)$, are (complex) functions which describe the resistance at position e. At the wall (i.e., $e = 1$), $\alpha_0(e)$ and $\alpha_1(e)$ attain finite limiting values of 0.52 and 0.27, respectively.[25] The exact expression of $\alpha_t(e)$ is unknown, but as it is of the order $k^{1/2}$ [25] it can be neglected for k values below 1, so Eq. 8 becomes:

$$k_{\text{wall}}(k) = 0.43\left(k^{\frac{5}{2}} + 2.89k^{\frac{3}{2}} + 2.01k^{\frac{1}{2}}\right) + \ldots \quad (\text{for } k < 1) \quad (10)$$

For k values larger than one, i.e. for small cross-sectional droplet head area[26,27]:

$$k_{\text{wall}} = 1.7 \quad (\text{for } k \geq 1). \quad (11)$$

Drag Coefficient and Hadamard Viscosity Correction Factor. The Reynolds numbers in our Y-junctions are typically between 0.1 and 10. In this Reynolds number range, liquid discs and spheres have comparable drag coefficients described as[21,23]:

$$C_D\Lambda = \frac{24}{\text{Re}_c}(1 + 0.14 \cdot \text{Re}_c^{0.7})\Lambda. \quad (12)$$

with:

$$\Lambda = \frac{3\lambda + 2}{3(\lambda + 1)}, \quad (13)$$

where λ is the (dynamic) viscosity ratio and Re_c is the Reynolds number of the continuous phase. These quantities are calculated as:

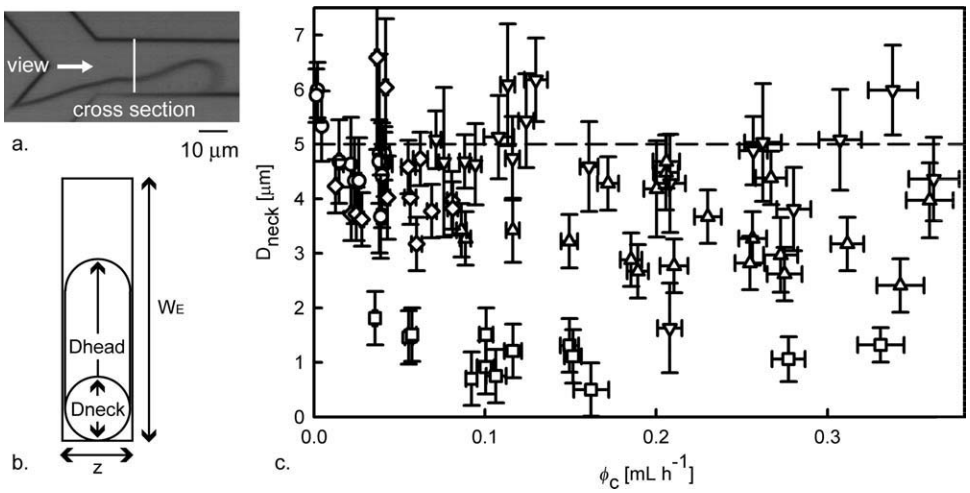

Figure 5. (a) Picture of the second-to-last frame before hexadecane droplet detachment in 20 wt % glycerol at ϕ_{G20} = 115 (± 5) μL h^{-1} and ϕ_{HD} = 4.5 (± 0.1) μL h^{-1}; the white line marks the position of the schematic cross-section shown in Figure 5b and the white arrow indicates the point of view; (b) schematic cross-section at the position where the neck is connected to the incipient droplet head (see Figure 5a); (c) the neck diameter D_{neck} as function of the glycerol–water flow rate ϕ_c for various disperse phases: 40 wt % pentane–hexadecane (▽), hexadecane (○), 60 wt % capric acid–hexadecane (□), low-viscous paraffin oil (△), and high-viscous paraffin oil (◇).

The dashed line indicates the channel depth.

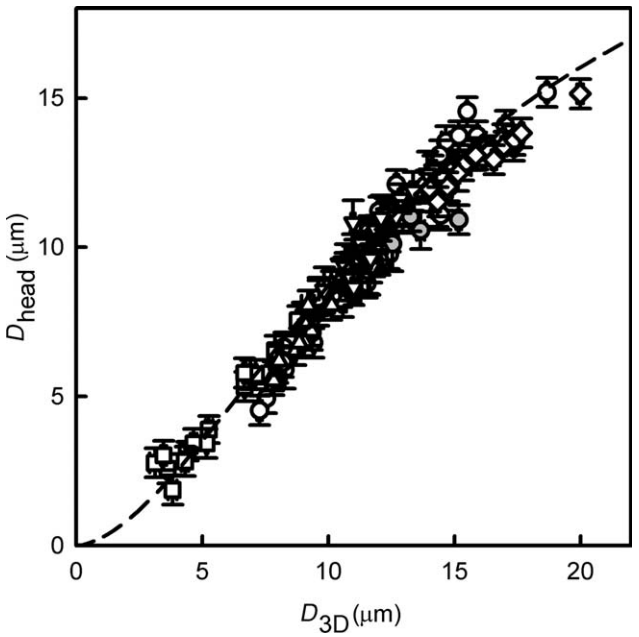

Figure 6. D_{head} as function of D_{3D} in the dripping and jetting regime at microfluidic Y-junctions for: 40 wt % pentane-hexadecane (▽), hexadecane (○), 60 wt % capric acid-hexadecane (□), low-viscous paraffin oil (△), and high-viscous-paraffin oil (◇) at various continuous- and disperse-phase flow rates, static interfacial tension, and continuous-phase viscosity as described in the experimental section.

The gray filled circles are for the smaller channel width. The dashed line is Eq. 18.

$$\lambda = \frac{\eta_d}{\eta_c} \tag{14}$$

and

$$\mathrm{Re}_c = \frac{\rho_c v_c D_{H,c}}{\eta_c}, \tag{15}$$

with

$$D_{H,c} = \frac{4(A_{\perp,E} - A_{\perp,neck})}{U_{\perp,E}} = \frac{2}{z + w_E}\left(z w_E - \frac{\pi}{4} D_{neck}^2\right), \quad (m) \tag{16}$$

where η_d and η_c are the disperse- and continuous-phase dynamic viscosity, respectively, $D_{H,c}$ is the hydraulic diameter of the area through which the continuous phase can flow past the neck, and $U_{\perp,E}$ is the perimeter of the downstream channel.

Force-Balance Model. From all the information mentioned in the section "Force-balance model development," droplet size follows from equating the interfacial tension force and the shear force (i.e. Eqs. 3 and 4):

$$\pi D_{neck} \gamma = 2\rho_c v_c^2 A_\perp(D_{head}) K_{wall}(D_{head}) C_D \Lambda. \tag{17}$$

This results in a complex equation, as both $A_\perp$ and K_{wall} are a function of D_{head}. Therefore, it was solved numerically with a script written in Matlab 7.0.1. This script determines F_{shear} for D_{head} values between 0 and 20 μm in steps of 0.1 μm and returns the D_{head} for which F_{shear} equals F_γ.

Equivalent Droplet Size. As a final step, the measured D_{head} (see section "droplet-formation quantities") is related to the experimental unrestricted droplet diameter D_{3D}, as droplet diameter is a more prevalent quantity. As the shape of the incipient droplet is complex (see e.g., Figure 5a) and not simply described by the deformation of an ellipse, we

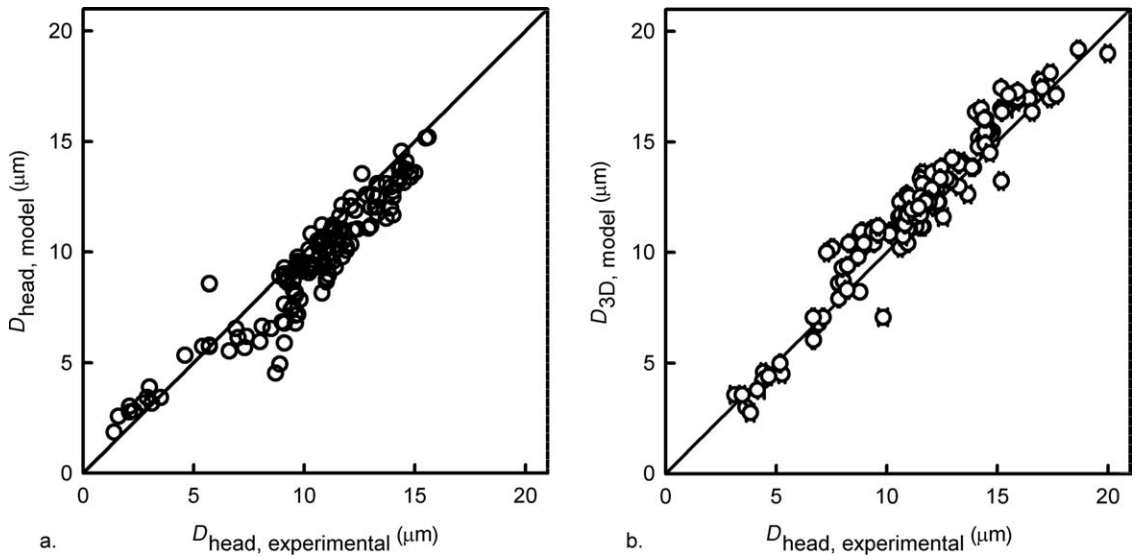

Figure 7. Comparison of D_{head} (a) and the droplet size D_{3D} (b) estimated with the force-balance model to the experimentally determined D_{head} and droplet size D_{3D} for various process conditions as described in the experimental section.

The diagonal line is the line of parity and the error bars represent the 95% confidence interval of the experimental droplet size.

Table 5. Standard Deviation Between the Force-Balance Model and the Data Points for the Complete Force-Balance Model (Eqs. 17 and 18), the Model Without the Viscosity or the Wall Correction Factor, and the Model Based on the Assumption that $D_{neck} = z$

Model	Standard Deviation* (μm)
Model following Eqs. 17 and 18	1.1
Model without viscosity correction factor	1.0
Model without wall correction factor	65.5
Model assuming D_{neck} equals z	2.1

*$\sqrt{(SS/(n-1)}$, with SS the sum of squares and n the number of data points.

derived an empirical relation through statistical analysis (implying no physical meaning):

$$D_{head} = \frac{1}{\frac{1}{a} + \frac{b}{D_{3D}^{c}}}, \quad (m) \tag{18}$$

where a, b, and c are the parameters fitted with the least squares method (see Experimental section). These parameters have a value (represented with their 95% confidence interval) of 25.6 ± 5.6, 3.8 ± 1.6, and 1.7 ± 0.2 for a, b, and c, respectively (see Figure 6).

Comparison model and experimental data

The force-balance model was compared with all 137 experimental Y-junction data, and Figures 7a, b show that all data were described adequately, irrespective of the considerable differences in disperse- and continuous-phase viscosity (η_d = 1.0–105.0 mPa s, η_c = 1.0–6.2 mPa s), flow rate (ϕ_d = 0.039–18.0 μL h^{-1}, ϕ_c = 1.39 μL h^{-1} to 0.41 mL h^{-1}), (static) interfacial tension (γ = 12–55 mN m^{-1}), and channel width (12.8–19.9 μm). Therewith, it is clear that the model has considerable predictive value and covers factors that were not implemented before. For droplets between 9 and 10 μm, a slight underestimation of the force-balance model can be observed for D_{head}; most probably this is caused by the changeover from one K_{wall} equation to the other (Eqs. 10 and 11).

The sensitivity of the force-balance model was tested by leaving out the viscosity correction factor Λ or the wall correction factor K_{wall}. The standard deviation between the so adjusted force-balance models and the data points was calculated. Table 5 shows that the influence of the viscosity correction factor is insignificant, especially, when compared to the effect of the wall correction factor. This finding strongly suggests that emulsification in Y-junctions is ruled by the resistance with the wall, and not by disperse-phase viscosity, or viscosity ratio, as is observed for other emulsification systems (e.g., see Figure 3).

As mentioned previously, the initial Y-junction model[15] assumed D_{neck} equal to the channel depth (z), but current results suggest that this is not always correct (see Figure 5c) and that is also reflected in the predicted droplet sizes. When it was assumed that $D_{neck} = z$, the standard deviation doubled (see Table 5). This suggests that the D_{neck} value is clearly essential for the description of the data points. Ideally, this value, which can only be determined experimentally, should become more accessible. For this, the contact angle between the microchannel wall and the liquids could be a starting point as it plausibly influences the shape of the neck, but unfortunately, this parameter is not (easily) accessible under the conditions studied here.

Conclusions

Microfluidic Y-junctions were used to produce monodisperse emulsions. A force-balance model was derived based on the cross-sectional area of the incipient droplet just before detachment from a neck with a cylindrical shape. The model shows good predictive value for emulsification in microfluidic Y-junctions in the dripping and jetting regime over a broad range of disperse- and continuous-phase viscosities, flow rates, and interfacial tensions. The model shows that the droplet size generated by Y-junctions is controlled by interfacial tension, continuous-phase properties (viscosity, density, and flow rate), and resistance with the wall and is practically independent of the disperse-phase viscosity and viscosity ratio. As droplet size is also not influenced by disperse-phase flow rate,[15] operation of Y-junctions is intrinsically simpler than other (shear-driven) microfluidic geometries.

Acknowledgments

The authors thank Anja Warmerdam for performing part of the experiments, Michael van Ginkel for writing the script for droplet analysis, and the MicroNed consortium for supporting this research.

Notation

Uppercase letters

$A_\perp$ = cross-sectional area of the incipient droplet head exposed to the continuous-phase flow (m^2)
$A_{\perp,E}$ = cross-sectional area of the downstream channel (m^2)
$A_{\perp,head}$ = cross-sectional area of the head (m^2)
$A_{\perp,neck}$ = cross-sectional area of the neck (m^2)
C_D = drag coefficient
Ca = capillary number of the continuous phase
D = diameter of a disc (m)
$D_{H,c}$ = the hydraulic diameter of the area through which the continuous phase can flow past the neck (m)
D_{head} = largest diameter of the incipient droplet head (m)
D_{neck} = diameter of the neck (m)
D_{3D} = equivalent diameter of an unrestricted spherical drop of the same volume as the droplet (m)
F_γ = interfacial tension force (N)
F_{shear} = shear force (N)
K_{wall} = wall correction factor
Re_c = Reynolds number of the continuous phase
R_{3D} = droplet radius (m)
SS = sum of squares
$U_{\perp,E}$ = perimeter of the downstream channel (m)
V = droplet volume (m^3)

Lowercase letters

a = fit parameter
b = fit parameter
c = fit parameter
e = measure for the position of the center of the droplet head compared to the wall

k = clearance between the channel and the droplet head
n = number of data points
v_c = (average) velocity of the continuous phase along the neck calculated with Eq. 5 (m s^{-1})
w_C = continuous-phase channel width (m)
w_D = disperse-phase channel width (m)
w_E = downstream-channel width (m)
z = depth of the Y-junction (m)

Greek letters

Λ = Hadamard viscosity correction factor
$\alpha_0(e)$ = (complex) function which describes the resistance at position e
$\alpha_1(e)$ = (complex) function which describes the resistance at position e
$\alpha_t(e)$ = (complex) function which describes the resistance at position e
ϕ_c = continuous-phase flow rate (m^3 s^{-1})
ϕ_d = disperse-phase flow rate (m^3 s^{-1})
ϕ_{G30} = flow rate of 30 wt % glycerol–water (m^3 s^{-1})
ϕ_{G20} = flow rate of 20 wt % glycerol–water (m^3 s^{-1})
ϕ_{HD} = flow rate of hexadecane (m^3 s^{-1})
ϕ_{LPO} = flow rate of low-viscous paraffin oil (m^3 s^{-1})
γ = interfacial tension (N m^{-1})
γ_c = shear rate of the continuous phase (s^{-1})
η = dynamic viscosity (Pa s)
η_c = dynamic viscosity of the continuous phase (Pa s)
η_d = dynamic viscosity of the disperse phase (Pa s)
λ = disperse-to-continuous-phase-viscosity-ratio
ρ = density (kg m^{-3})
ρ_c = density of the continuous phase (kg m^{-3})

Literature Cited

1. Schröder V, Schubert H. Production of emulsions using microporous, ceramic membranes. *Colloids Surf A*. 1999;152:103–109.
2. McClements DJ. *Food Emulsions—Principles, Practices and Techniques*, 2nd ed. Boca Raton, FL: CRC Press, 2005.
3. Joscelyne SM, Trägårdh G. Food emulsions using membrane emulsification: conditions for producing small droplets. *J Food Eng*. 1999;39:59–64.
4. Zhao Y, Chen G, Yuan Q. Liquid-liquid two-phase flow patterns in a rectangular microchannel. *AIChE J*. 2006;52:4052–4060.
5. Tice JD, Lyon AD, Ismagilov RF. Effects of viscosity on droplet formation and mixing in microfluidic channels. *Anal Chim Acta*. 2004;507:73–77.
6. Thorsen T, Roberts RW, Arnold FH, Quake SR. Dynamic pattern formation in a vesicle-generating microfluidic device. *Phys Rev Lett*. 2001;86:4163–4166.
7. Nisisako T, Torii T, Higuchi T. Novel microreactors for functional polymer beads. *Chem Eng J*. 2004;101:23–29.
8. van der Graaf S, Steegmans MLJ, van der Sman RGM, Schroën CGPH, Boom RM. Droplet formation in a T-shaped microchannel junction: a model system for membrane emulsification. *Colloids Surf A*. 2005;266:106–116.
9. Garstecki P, Fuerstman MJ, Stone HA, Whitesides GM. Formation of droplets and bubbles in a microfluidic T-junction—scaling and mechanism of break-up. *Lab Chip*. 2006;6:437–446.
10. De Menech M, Garstecki P, Jousse F, Stone HA. Transition from squeezing to dripping in a microfluidic T-shaped junction. *J Fluid Mech*. 2008;595:141–161.
11. Steegmans MLJ, Schroën CGPH, Boom RM. Generalised insights in droplet formation at T-junctions through statistical analysis. *Chem Eng Sci*. 2009;64:3042–3050.
12. Capretto L, Mazzitelli S, Balestra C, Tosi A, Nastruzzi C. Effect of the gelation process on the production of alginate microbeads by microfluidic chip technology. *Lab Chip*. 2008;8:617–621.
13. Kawai A, Matsumoto S, Kiriya H, Oikawa T, Hara K, Ohkawa T, Futami T, Katayama K, Nishizawa K. Development of a microreactor for manufacturing gel particles without glass selection of diameter. *TOSOH Res Technol Rev*. 2003;47:3–9.
14. Kubo A, Shinmori H, Takeuchi T. Atrazine-imprinted microspheres prepared using a microfluidic device. *Chem Lett*. 2006;35:588–589.
15. Steegmans MLJ, Schroën CGPH, Boom RM. Characterization of emulsification at flat microchannel Y-junctions. *Langmuir*. 2009;25:3396–3401.
16. Grace HP. Dispersion phenomena in high viscosity immiscible fluid systems and application of static mixers as dispersion devices in such systems. *Chem Eng Commun*. 1982;14:225–277.
17. Nie Z, Seo M, Xu S, Lewis PC, Mok M, Kumacheva E, Whitesides GM, Garstecki P, Stone HA. Emulsification in a microfluidic flow-focusing device: effect of the viscosities of the liquids. *Microfluid Nanofluidics*. 2008;5:585–594.
18. Cristobal G, Arbouet L, Sarrazin F, Talaga D, Bruneel JL, Joanicot M, Servant L. On-line laser Raman spectroscopic probing of droplets engineered in microfluidic devices. *Lab Chip*. 2006;6:1140–1146.
19. Benjamins J, Cagna A, Lucassen-Reynders EH. Viscoelastic properties of triacylglycerol/water interfaces covered by proteins. *Colloids Surf A*. 1996;114:245–254.
20. Guillot P, Colin A, Ajdari A. Stability of a jet in confined pressure-driven biphasic flows at low Reynolds number in various geometries. *Phys Rev E Stat Nonlin Soft Matter Phys*. 2008;78:016307-1–016307-13.
21. Green DW, Perry RH. *Perry's Chemical Engineers' Handbook*, 8th ed. New York: McGraw-Hill, 2007.
22. Shintaku H, Kuwabara T, Kawano S, Suzuki T, Kanno I, Kotera H. Micro cell encapsulation and its hydrogel-beads production using microfluidic device. *Microsyst Technol*. 2007;13:951–958.
23. Husny J, Cooper-White JJ. The effect of elasticity on drop creation in T-shaped microchannels. *J Non-Newtonian Fluid Mech*. 2006;137:121–136.
24. Chang YC, Keh HJ. Slow motion of a slip spherical particle perpendicular to two plane walls. *J Fluids Struct*. 2006;22:647–661.
25. Bungay PM, Brenner H. The motion of a closely-fitting sphere in a fluid-filled tube. *Int J Multiphase Flow*. 1973;1:25–56.
26. O'Neill ME. A sphere in contact with a plane wall in a slow linear shear flow. *Chem Eng Sci*. 1968;23:1293–1298.
27. Bungay PM, Brenner H. Pressure drop due to the motion of a sphere near the wall bounding a Poiseuille flow. *J Fluid Mech*. 1973;60:81–96.

Manuscript received July 21, 2009, and revision received Dec. 9, 2009.